TUDelft

Delft University of Technology

A high responsivity and controllable recovery ultraviolet detector based on a WO$_3$ gate AlGaN/GaN heterostructure with an integrated micro-heater

Sun, Jianwen; Zhang, Shuo; Zhan, Teng; Liu, Zewen; Wang, Junxi; Yi, Xiaoyan ; Li, Jinmin; Sarro, Pasqualina M.; Zhang, Guoqi

Important note
To cite this publication, please use the final published version (if applicable).
Please check the document version above.

Showcasing research from R&D Center for Solid State Lighting, Institute of Semiconductors, Chinese Academy of Sciences, P.R. China and Department of Microelectronics, Delft University of Technology, the Netherlands

A high responsivity and controllable recovery ultraviolet detector based on a WO₃ gate AlGaN/GaN heterostructure with an integrated micro-heater

The UV detection, high responsivity, high stability, controllable recovery process and low production cost make AlGaN/GaN heterostructure photodetectors extremely attractive for several applications, such as fire detection, environmental monitoring and healthcare.

ROYAL SOCIETY
OF **CHEMISTRY**

rsc.li/materials-c

Registered charity number: 207890

PAPER

Check for updates

A high responsivity and controllable recovery ultraviolet detector based on a WO₃ gate AlGaN/GaN heterostructure with an integrated micro-heater†

Jianwen Sun, [ID] ‡[a] Shuo Zhang,‡[bc] Teng Zhan, [ID] *[bc] Zewen Liu,[d] Junxi Wang,[bc] Xiaoyan Yi,*[bc] Jinmin Li,[bc] Pasqualina M. Sarro*[a] and Guoqi Zhang*[ae]

A high responsivity and controllable recovery ultraviolet (UV) photodetector based on a tungsten oxide (WO₃) gate AlGaN/GaN heterostructure with an integrated micro-heater is reported for the first time. The WO₃ nanolayer was deposited by physical vapor deposition (PVD) for deep UV absorption and the micro-heater was integrated for chip level heating and cooling. Our device when exposed to UV wavelength exhibits a high responsivity of 1.67×10^4 A W^{-1} at 240 nm and a sharp cut-off wavelength of 275 nm. More importantly, the persistent photoconductivity (PPC) effect can be eliminated by a novel method, mono-pulse heating reset (MHR), which consists in applying an appropriate pulse voltage to the micro-heater right after the removal of the UV illumination. The recovery time was reduced from hours to just seconds without reducing the high responsivity and stability of the photodetector. The UV detection, high responsivity, high stability, controllable recovery process and low production cost of GaN-based photodetectors make these devices extremely attractive for several applications, such as fire detection and missile and rocket warning.

Introduction

Ultraviolet light is electromagnetic radiation with a wavelength from 100 nm to 400 nm, which can be divided into three ranges: UVC (100–280 nm), UVB (280–315 nm), UVA (315–400 nm). Levels of ozone around the earth block different bands of ultraviolet radiation. UVA is hardly affected by ozone and most of it reaches the surface of the earth. In contrast, UVC is strongly absorbed by the ozone layer and atmosphere, and UVB is also mostly absorbed by the ozone layer. Solar-blind region irradiation is almost non-existent in the atmosphere near the ground. Hence, solar-blind photodetectors are specifically needed in applications like fire sensing, missile and rocket warning, non-line-of sight optical communication, ozone monitoring, and so on.[1–5]

Numerous types of semiconductor detector structures have been reported, such as Schottky barrier photodiodes,[6] metal–semiconductor–metal (MSM) type photodetectors,[7] photoconductors, and p–n junction type and p–i–n photodiodes[8] for ultraviolet light detection. These different types of structures have different working mechanisms, cost and characteristics, which determine their commercial applications.[9,10] The performance of photodetectors is usually dependent on the semiconductor material used, such as traditional wide-bandgap semiconductors, III-nitride semiconductors, and metallic oxides. Wide-bandgap semiconductors include SiC and some group III–V compounds with ≈ 3.1 eV bandgap and ≈ 400 nm cutoff wavelength. Metal oxide materials include zinc oxide (ZnO),[11,12] titanium dioxide (TiO₂),[13,14] stannic oxide (SnO₂),[15,16] vanadium oxide (VO₂),[17] gallium trioxide (Ga₂O₃),[18–20] and WO₃.[21–24] In recent years, WO₃ has been widely used as a functional material in ultraviolet photodetectors.[22–24] Among the most frequently used III-nitride semiconductors are gallium nitride (GaN),[25,26] aluminium gallium nitride (AlGaN),[27,28] aluminum nitride (AlN),[1,29] indium nitride (InN)[30] and boron nitride (BN).[31] AlGaN/GaN heterostructures or AlGaN-based ultraviolet photodetectors with different structures have been widely investigated.[27,28,32–35] Solar-blind detection requires epitaxial layers with higher Al content.[36,37] However, epitaxial growth of AlGaN with high Al content is extremely difficult. To realize high performance AlGaN-based UV detectors, more complex processes and higher costs will therefore be required.[25,36,38–40]

[a] *Department of Microelectronics, Delft University of Technology, 2628 CD Delft, The Netherlands. E-mail: p.m.sarro@tudelft.nl, G.Q.Zhang@tudelft.nl*

[b] *Research and Development Center for Solid State Lighting, Institute of Semiconductors, Chinese Academy of Sciences, Qinghua East Road 35A, 100083, Beijing, China. E-mail: zhanteng10@semi.ac.cn, spring@semi.ac.cn*

[c] *College of Materials Sciences and Opto-Electronic Technology, University of Chinese Academy of Sciences, No. 19A Yuquan Road, Beijing, 100049, China*

[d] *Institute of Microelectronic, Tsinghua University, 100084, Beijing, China*

[e] *Shenzhen Institute of Wide-Bandgap Semiconductor, 518071, Shenzhen, China*

† Electronic supplementary information (ESI) available. See DOI: 10.1039/d0tc00553c

‡ Jianwen Sun and Shuo Zhang contributed equally to this paper.

An ideal photodetector would exhibit a low dark current to minimize the interference noise and high responsivity to maximize the photosignal. Currently, an avalanche-type detector[41–43] can obtain high responsivity but at the expense of increased noise and highly demanding requirements of structure and processing techniques. Another common approach to improve responsivity is to use the photoconductive type, which is easy to fabricate at lower cost and has a good commercial prospect. However, photodetectors with photoconductive gain usually have a persistent photoconductivity (PPC) effect[44–46] due to the capture of photo-generated carriers on defects. The PPC effect severely affects the recovery time of these photodetectors, values measured range from hours to days[46] after the removal of UV illumination. This poses a big challenge for detecting the change of light intensity at high frequency. Many methods were employed to reduce the PPC effect, such as infrared irradiation, electric field, and pulsed voltage.[47–51] Besides these methods, heating the device has been recently reported to suppress the PPC effect in GaN-based or Ga_2O_3-based detectors. Hou et al. presented a special method for suppressing the PPC effect in AlGaN/GaN photo-detectors by applying in situ heating.[34]

Sun et al. proposed that continuously pulsed heating can reduce the decay time of a suspended AlGaN/GaN heterostructure photodetector by 30–45% compared to the DC heating mode.[35] However, neither in situ heating nor continuously pulsed heating can suppress the PPC effect completely. The decay time is just reduced from days or several hours to hundreds of seconds. Zhou et al. demonstrated that the "thermal relaxation" process can effectively reduce the recovery time of an α-Ga_2O_3 detector from hours to seconds.[52] But the thermal relaxation process required the detector to be placed on a hot plate for heating and then removed to a heat sink for cooling. These operations may make the detector unsuitable for practical application. Therefore, a simple, effective and universal method is urgently needed for a simple and easy to fabricate photodetector with high responsivity and fast recovery. In this research, we employed the physical vapor deposition (PVD) method to grow a WO_3 nanolayer on an AlGaN/GaN epitaxial heterostructure. At the same time, a Ti/Pt micro-heater was integrated around the 2DEG area of the AlGaN/GaN device, which enables the detector to be heated and cooled at the chip level without additional operations. This novel structure device exhibits high responsivity under UV illumination and controllable recovery characteristics using mono-pulse heating reset (MHR) after the removal of UV light. The peak responsivity is 16 700 A W^{-1} at 240 nm, and the sharp cut-off wavelength is 275 nm. The mechanisms of PPC and its elimination are illustrated and discussed here.

Experimental

Epitaxial materials

The AlGaN/GaN epitaxial heterostructure was grown on a $\langle 111 \rangle$ silicon wafer, 100 mm in diameter and 1 mm in thickness, using Metal–Organic Chemical Vapor Deposition (MOCVD). The epitaxial structure consisted of an undoped GaN buffer layer (2 μm), followed by an AlN interlayer (1 nm), an undoped $Al_{0.26}Ga_{0.74}N$ barrier layer (25 nm), and a 3 nm GaN cap layer. The electron mobility of the 2DEG was $\sim$1500 cm^2 V^{-1} s^{-1}, with a sheet electron density of $\sim$1 $\times$ 10^{13} cm^{-2}.
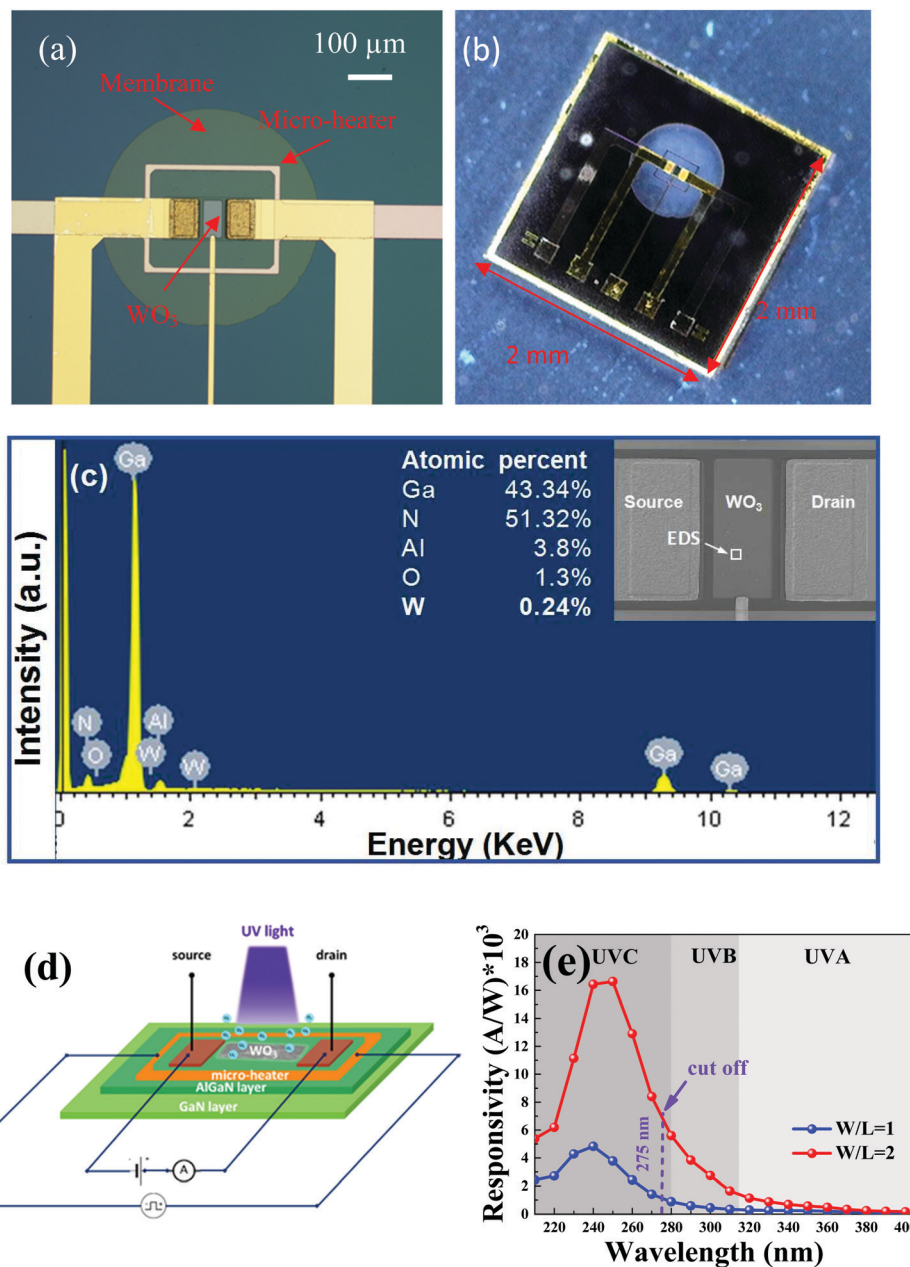
Device fabrication

The fabrication process started with mesa etching using chlorine/boron chloride (Cl_2/BCl_3) inductively coupled plasma reactive ion etching (ICP-RIE) to define the sensor geometry. Then, Ti/Al/Ti/Au (20/110/40/50 nm) metal contacts were e-beam evaporated and patterned by lift-off technology. After patterning, the contacts were subjected to a rapid thermal anneal at 870 °C for 45 s under N_2 ambient. A 200 nm silicon dioxide (SiO_2) layer was then deposited by plasma-enhanced chemical vapor deposition (PECVD). A Ti/Pt (30/200 nm) metal layer was e-beam evaporated and patterned by lift-off to form the micro-heater, followed by a 200 nm PECVD SiO_2 layer for isolation from the interconnect layer. After opening windows in the SiO_2 layer, the metal inter-connect was formed using an evaporated Ti/Au (20/300 nm) layer stack. The topside of the wafer was covered with the PECVD SiO_2 layer and the backside was polished down to 400 μm. A 5 μm-thick SiO_2 layer on the backside of the wafer as a hard mask during the DRIE process to etch the silicon substrate was deposited and patterned by ICP etching. The topside SiO_2 layer was etched in BOE solution to open the contact pads and gate windows.

The WO_3 (10 nm) layer was deposited on the gate area of 40 μm × 80 μm by physical vapor deposition (PVD). The silicon substrate is etched away below the active area in the final step. The microheater has a rectangular geometry around a central area of 230 μm × 290 μm, as shown in Fig. 1(a). Fig. 1(b) shows the optical image of the complete WO_3/AlGaN/GaN heterostructure detector with a size of 2 mm × 2 mm. The schematic drawing of the cross-section of the device is shown in the ESI,† Fig. S1.

Measurements

The spectral response of the AlGaN/GaN photodetectors was measured in a spectrometer testing DSR200 system (Zolix Instrument Co., Ltd, China). It was exposed to monochromatic light with wavelength from 200 to 400 nm at a drain–source voltage of 0.5 V, controlled by a Keithley 2400, in air ambient at room temperature. The illuminating source was a 150 W xenon lamp.

The surface membrane temperature of the photodetector is modulated by Joule heating of the micro-heater when the current flows through the Ti/Pt layer. To calculate the membrane temperature, a calibration is performed according to previously reported measurement results;[53] the surface temperatures of the device in the working mode (V_{DS} = 0.5 V) are 60 °C, 80 °C, 100 °C and 120 °C when voltages of 2.1 V, 2.7 V, 3.2 V and 3.7 V, respectively, are applied to the microheater. The thermal distribution of the surface of the photodetector is given in the ESI,† Fig. S2. The mono-pulse heating reset (MHR) process was performed by controlling the voltage of the micro-heater. The peak wavelengths (λ_p) of the UVC and UVA LED light sources are 268.2 nm and 395.1 nm, and the full width at half maximum (FWHM) values are 9.1 nm and 11 nm, respectively. More information about UVC and UVA LED chips are given in the ESI,† Fig. S3 and S4.

5410 | J. Mater. Chem. C, 2020, **8**, 5409–5416

This journal is © The Royal Society of Chemistry 2020

Fig. 1 The enlarged active part (a) and the optical image (b) of the WO_3/AlGaN/GaN photodetector; (c) EDS spectra of the device gate surface and the SEM image (inset); (d) schematic illustration of the WO_3/AlGaN/GaN heterostructure photodetector with an integrated micro-heater; (e) measured spectral response of the WO_3/AlGaN/GaN heterostructure photodetector.

Results and discussion

Fig. 1(c) presents the energy dispersive spectroscopy (EDS) spectra of the gate surface of the detector for the binding energy range from 0 keV to 12 keV. The percentage of Ga, N, Al, O, and W is 43.34%, 51.32%, 3.8%, 1.3% and 0.24%, respectively. Clearly, the deposition of WO_3 on the gate surface by magnetron sputtering PVD is confirmed. More details about the structure and fabrication process of our device could been found in our earlier publications.[35,53,54] Fig. 1(d) shows a schematic illustration of the WO_3/AlGaN/GaN heterostructure

photodetector with the integrated micro-heater. The measured spectral response of the WO_3/AlGaN/GaN heterostructure photodetector shows high responsivity in the UVC range (wavelength of 210–280 nm). The peak responsivity of the photodetector with $W/L = 2$ was 16 700 A W^{-1} at 0.5 V bias under 240 nm illumination, as shown in Fig. 1(e), which exceeds 100% quantum efficiency due to the high gain of the HEMT 2-dimensional electron gas (2EDG) structure. A sharp cutoff wavelength of the photodetector defined as the ratio between the maximum responsivity and the natural constant ($e \approx 2.718$) is located at 275 nm (<280 nm).[55,56] The excellent performance

This journal is © The Royal Society of Chemistry 2020
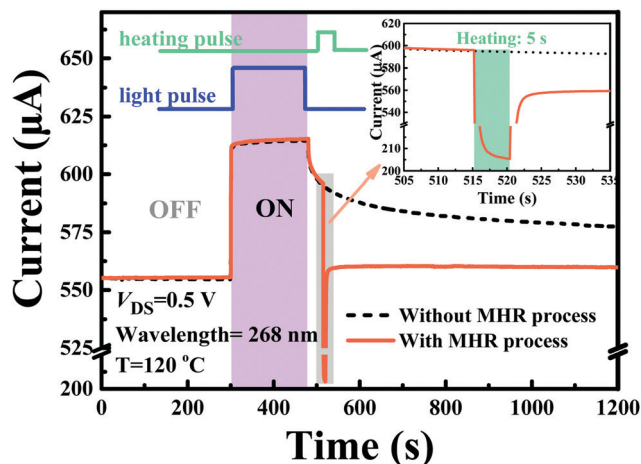
J. Mater. Chem. C, 2020, **8**, 5409–5416 | **5411**

Fig. 2 The transient response of a WO$_3$ gate AlGaN/GaN heterostructure photodetector to 268 nm UV illumination and the removal of the PPC effect by the novel MHR methods: heating reset (inset).

of our devices is a clear indication of the potential applicability of this configuration for ultraviolet photodetectors.

Fig. 2 shows the transient response characteristics of the WO$_3$/AlGaN/GaN heterostructure photodetector under 268 nm light illumination at a bias of 0.5 V. Upon exposure to UV illumination, the photocurrent increases immediately. The dark current and UV illumination current of the photodetector were 554 μA and 614 μA, respectively. Upon removal of the UV illumination, the drain current slowly decays with a decay time of several hours (black dashed line). A similar decay phenomenon was observed under different UV illumination intensities and different wavelengths as shown in Fig. 3 and 4. This long recovery process was due to the energy barrier that delays the recombination of photogenerated carriers (PPC effect). Thus, the PPC effect has to be suppressed in order to realize fast recovery of the photodetector.

As shown in Fig. 2 (red solid line inset), after removing the UV illumination, the photodetector was heated to 120 °C for 5 seconds by applying an integrated micro-heater voltage of 3.7 V, and then cooled down to room temperature (about 20 °C) for 2 seconds. Interestingly, the dark current first dropped rapidly to 205 μA due to the carrier scattering in the 2DEG channel by increasing the temperature of the WO$_3$/AlGaN/GaN

heterostructure photodetector, then came back to 560 μA after the MHR process and remained stable. The same behaviour was observed for different intensities as well, as shown in Fig. 3, 4 and 6. This finding means that the PPC effect is eliminated by this short MHR process, and the decay time is reduced from hours to <7 seconds.

In order to further optimize the MHR process, the transient photocurrent response of the WO$_3$/AlGaN/GaN heterostructure photodetector under the MHR process for different temperatures was measured. The results are shown in Fig. 3. The value at which the current stabilizes after the MHR process decreased with the temperature, which means that the suppression of the PPC effect can be effectively accelerated by increasing the operating temperature of the photodetector. The trapped photogenerated carriers get more thermal energy with increasing temperature, and their capture increases, resulting in the decrease of the dark current. The stable current basically remains constant when the temperature of MHR is above 80 °C, which means that the PPC effect is almost eliminated. Although the PPC effect would slightly decrease with increasing MHR temperature, the decay time is the same, while the power consumption of the micro-heater would be much higher. Therefore, for our samples, 80 °C is sufficient to remove the PPC effect.

Fig. 4 shows the time dependent drain current of the WO$_3$/AlGaN/GaN photodetector under UVA and UVC light illumination, respectively. The PPC effect is effectively eliminated by this novel method: mono-heating reset (MHR) under different light wavelengths and light intensities. In Fig. 4(a)–(c), the stable dark current after the MHR process was lower than that before UVA illumination, possibly because of the trapped carriers in defects. A small increase under higher light intensity is observed, as shown in Fig. 4(b), due to the increase in photogenerated carriers at higher intensity. The change of photocurrent to dark current versus light power or intensity as shown in Fig. 4(c) could also support this phenomenon. As shown in Fig. 4(d)–(f), the photocurrent change increases with the UVC light intensity and then reaches a saturation value. The response time decreases with the light intensity as shown in Fig. 4(f). When the light intensity is 20.3 μW cm^{-2}, the measured response time is 0.7 s. These measurement results indicate that higher UV intensity results in more photogenerated carriers at a faster rate.
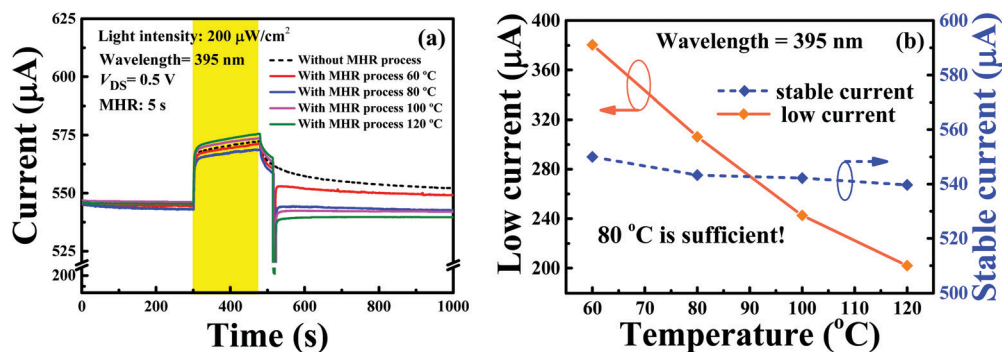

Fig. 3 (a) The transient photocurrent response of the WO$_3$/AlGaN/GaN heterostructure detector measured with the MHR process at different temperatures and at V_{DS} = 0.5 V. (b) The low drain current and stable current with the MHR process at different temperatures.
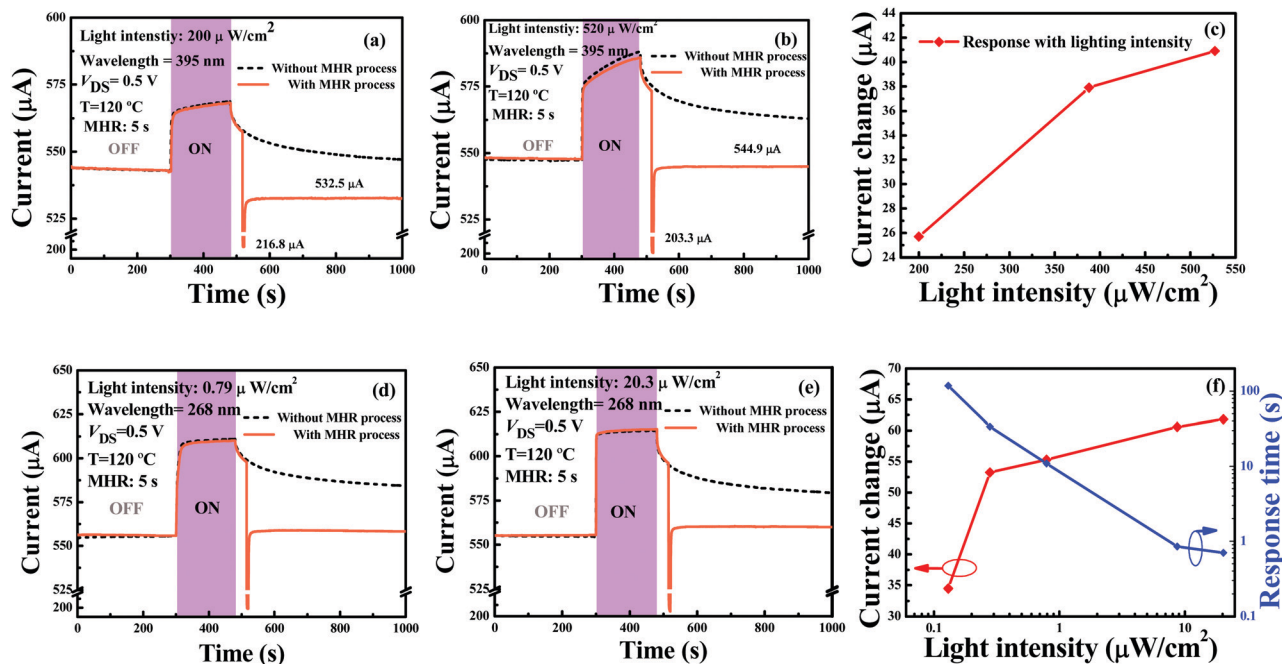
Fig. 4 The transient response of a WO$_3$ gate AlGaN/GaN heterostructure photodetector to 395 nm UV illumination and the PPC effect that can be removed by the MHR process: short heating reset at different illumination intensities (a) 200 μW cm^{-2} and (b) 520 μW cm^{-2}; (c) drain current change *versus* light intensity; the transient response to 268 nm UV illumination: short heating reset at different illumination intensities (d) 0.79 μW cm^{-2} and (e) 20.3 μW cm^{-2}; (f) drain current change and response time *versus* light intensity.

WO$_3$ is an n-type semiconductor[22,23] and Fig. 5 shows the corresponding UV sensing and PPC mechanisms on the energy band diagram. When there is no bias applied between the source and drain of the detector in the dark, the oxygen molecules from the ambient air absorbed on the nanolayer WO$_3$ combine with electrons and create a depletion sub-layer near the surface [O$_2$(gas) + e$^-$ → O$_2^-$(adsorb)], where O$_2^-$ is the adsorbed oxygen ion on the WO$_3$ surface, so that there is a depletion layer at the
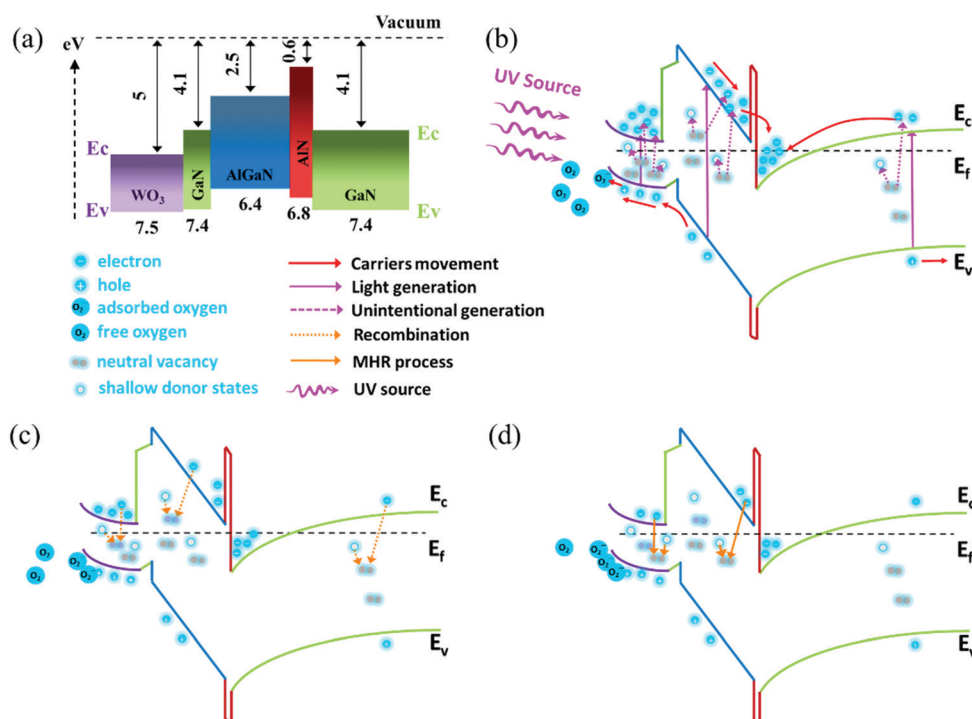

Fig. 5 (a) Schematic illustration of the energy band diagrams to describe the WO$_3$/AlGaN/GaN heterostructure photodetector. (b) Under UV illumination; (c) upon removal of UV illumination; (d) MHR process. E_f and dashed line denote the Femi level.

nanolayer WO_3 surface, as shown in Fig. 5. Under the UV light illumination conditions, more electron–hole pairs are photogenerated inside WO_3, as shown in Fig. 5(b). Then the generated holes move towards the WO_3 surface to recombine with the electrons trapped in O_2^- ions [$h^+ + O_2^-$(adsorb) $\rightarrow O_2$(gas)],[22] which helps the adsorbed oxygen ions to desorb from the WO_3 surface and decrease the width of the depletion layer. Therefore, the negative potential on the WO_3 nanolayer is reduced and the 2DEG concentration in the channel layer of the heterostructure is enhanced. Meanwhile, the generated carriers in AlGaN and GaN layers also move to the 2EDG quantum well,[57] as shown in Fig. 5(b). On the other hand, the neutral vacancy can be ionized to the shallow donor state under light illumination.[52] And the electrons in the band tail states are also excited to the conduction band. Hence, the drain–source current of the photodetector is increased under UV illumination. After the UV illumination, the energy barrier delays the recombination of the photogenerated carriers, which results in a long recovery time (PPC effect). Only a few of the photogenerated electrons could recombine with the holes and the shallow donor state as shown in Fig. 5(c). In order to suppress the PPC effect, the MHR process was conducted as shown in Fig. 5(d). The electrons in the band tail states under the conduction band are easily excited and provide more free electrons, and the higher electron concentration accelerates the recombination of carriers. Meanwhile, the electrons get more thermal energy to overcome the energy barrier and increase the

capture rate at high temperature. On the other hand, under the MHR process, more oxygen molecules from the ambient air are absorbed on the surface of the WO_3 nanolayer, combine with electrons and increase the depletion layer. Thus, the negative potential on the WO_3 nanolayer is raised and the 2DEG concentration in the channel layer of the heterostructure is decreased. Therefore, after the MHR process, the number of O^- on the WO_3 nanolayer and the width of the depletion layer are back to the original level before UV illumination. As a result, compared to the current of the photodetector without the MHR process, the dark current is recovered and it remains stable. The PPC effect is suppressed.

Fig. 6(a)–(d) show the transient photocurrent response of the WO_3/AlGaN/GaN heterostructure photodetector with and without the MHR process under UVA (395 nm) and UVC (268 nm) illumination. The MHR process is a 5 second heating pulse. As shown in the upper part of Fig. 6(a)–(d), after the first on/off cycle of UV light, the photocurrent decays slowly and does not recover to the initial value. Then the light current increases slightly after further cycles. By contrast, the PPC effect was clearly suppressed by the MHR process, as shown in the lower part of Fig. 6(a)–(d). After six cycles the photocurrent of the photodetector still maintains consistency and repeatability. The decay time is about 7 seconds including 5 seconds of the MHR process and 2 seconds of dark current recovery. The photo-response of our device under the same light intensity (Fig. 6a and c) and different light
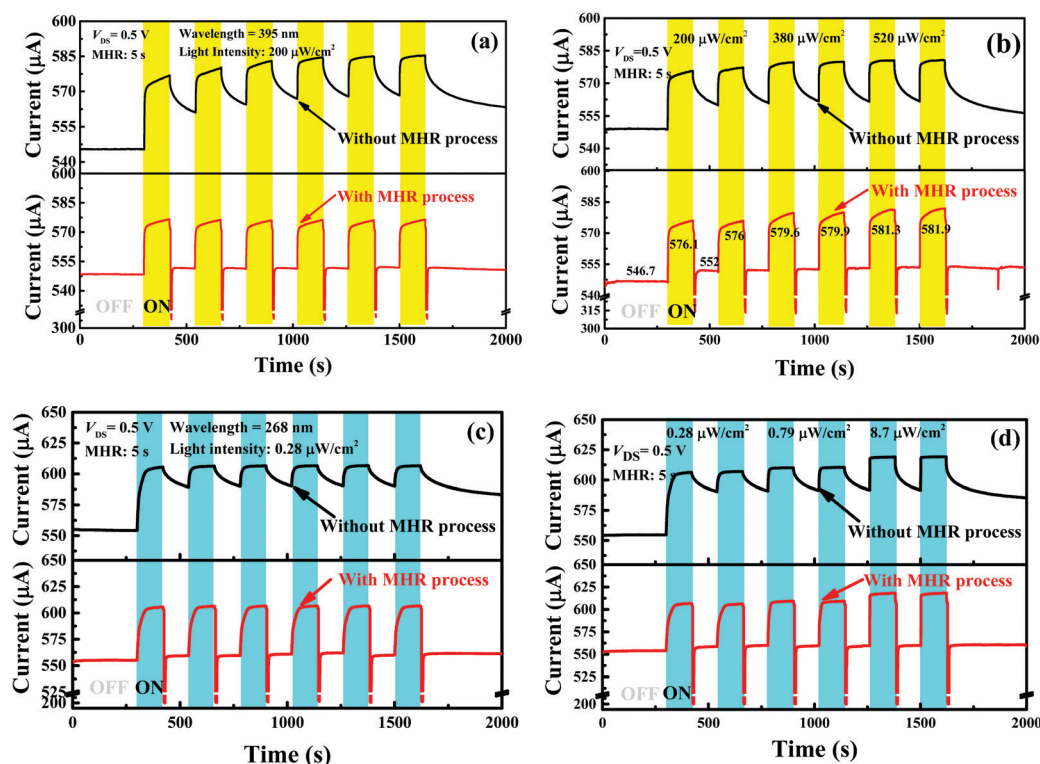
Fig. 6 The transient photocurrent response of the WO_3/AlGaN/GaN heterostructure photodetector measured under 395 nm illumination at $V_{DS} = 0.5$ V. (a) Six cycles at a light intensity of 200 μW cm^{-2}; (b) every two cycles at different light intensities (200 μW cm^{-2}; 380 μW cm^{-2} and 520 μW cm^{-2}). The transient photocurrent response of the WO_3/AlGaN/GaN heterostructure photodetector measured under 268 nm illumination at $V_{DS} = 0.5$ V; (c) six cycles at a light intensity of 0.28 μW cm^{-2}; (d) every two cycles at different light intensities (0.28 μW cm^{-2}; 0.79 μW cm^{-2}; 8.7 μW cm^{-2}).

5414 | *J. Mater. Chem. C*, 2020, **8**, 5409–5416

This journal is © The Royal Society of Chemistry 2020

Table 1 Comparison of the parameters of GaN-based photodetectors

Photodetector	Wavelength (nm)	Peak responsivity (A W^{-1})	Recovery time	Ref.
WO$_3$/AlGaN/GaN	200–395	1.67×10^4 (0.5 V)	7 s	This work
V-Grooved AlGaN/GaN	365	4×10^{-4} (1 V)	34 s	32
AlGaN/GaN	365	—	24 s	34
Ga$_2$O$_3$/AlGaN/GaN	250–450	30 (−5 V)	∼100 s	58
Graphene/AlGaN/GaN	250–375	0.56 (−2 V)	13.8 s	33
p-NiO/GaN	280–380	∼0.2 (−1)	35 ms	59
InAlN/GaN	300–367	32.9 (5 V)	3–4 ms	60
GaN nanoflowers	325	10.5 (1 V)	27 ms	61
Pt–GaN nanowire	380	6.39×10^4	0.65 s	62
GaN/Ga$_2$O$_3$	254; 365	28.4×10^{-3}; 54.43×10^{-3}	0.08 s; 0.12 s	63
GaN porous film	300–380	0.315	0.03 s	64
Single InGaN/GaN wire	244; 360; 488	8×10^3	3000 s	65

intensities (Fig. 6b and d) are measured. These results indicate that the MHR process could make it possible to realize the WO$_3$/AlGaN/GaN 2DEG structure photodetectors with high responsivity and fast response/recovery at the same time. The MHR process enables the detector to be heated and cooled at the chip level, which makes WO$_3$/AlGaN/GaN heterostructure photodetectors suitable for practical applications. And from the example shown in Fig. S5 (ESI†), the MHR process would be as a start process before the UV measurement to obtain the initial dark current. During the UV measurement, the MHR process would be used to speed up the recovery time. Then, the photodetector would make a new measurement again.

Table 1 shows a comparison of the parameters of GaN-based photodetectors. It can be seen that our WO$_3$/AlGaN/GaN heterostructure photodetector has a higher responsivity than most reported detectors. Moreover, our detector offers at the same time high responsivity and controllable recovery under UV illumination, thanks to the implementation of the MHR process.

Conclusions

In summary, a WO$_3$/AlGaN/GaN heterostructure photodetector with an integrated micro-heater was micro-fabricated and characterized. We employed the physical vapor deposition (PVD) method to grow a WO$_3$ nanolayer on the AlGaN/GaN epitaxial heterostructure for deep UV absorption. An integrated micro-heater around the 2DEG area of the AlGaN/GaN device enabled a mono-pulsed heating process at the chip scale without the need for external heating. Our devices respond to the UV wavelength and exhibit a high responsivity of 1.67×10^4 A W^{-1} at 240 nm, with a sharp cut-off wavelength of 275 nm. Importantly, the persistent photoconductivity (PPC) effect can be eliminated by the novel method introduced here: mono-pulse heating reset (MHR) by applying a pulse voltage to the micro-heater after the removal of the UV illumination. The recovery time was reduced from hours to seconds without reducing the high responsivity and without affecting the stability of the photodetector. The UV detection, high responsivity, controllable recovery process and low production cost make the AlGaN/GaN heterostructure photodetectors suitable for commercial applications.

Conflicts of interest

There are no conflicts to declare.

Acknowledgements

Notes and references

1 W. Zheng, F. Huang, R. Zheng and H. Wu, *Adv. Mater.*, 2015, **27**, 3921–3927.
2 M. Razeghi and A. Rogalski, *J. Appl. Phys.*, 1996, **79**, 7433–7473.
3 Z. Y. Xu and B. M. Sadler, *IEEE Commun. Mag.*, 2008, **46**, 67–73.
4 Y. Zou, Y. Zhang, Y. Hu and H. Gu, *Sensors*, 2018, **18**, 2072.
5 J. Xu, W. Zheng and F. Huang, *J. Mater. Chem. C*, 2019, **7**, 8753–8770.
6 L. Sang, M. Liao, Y. Koide and M. Sumiya, *Appl. Phys. Lett.*, 2011, **99**, 031115.
7 P. F. Satterthwaite, A. S. Yalamarthy, N. A. Scandrette, A. Newaz and D. G. Senesky, *ACS Photonics*, 2018, **5**, 4277–4282.
8 W. Xu, Y. Shi, F. Ren, D. Zhou, L. Su, Q. Liu, L. Cheng, J. Ye, D. Chen and R. Zhang, *Photonics Res.*, 2019, **7**, B48–B54.
9 C. Xie, X. T. Lu, X. W. Tong, Z. X. Zhang, F. X. Liang, L. Liang, L. B. Luo and Y. C. Wu, *Adv. Funct. Mater.*, 2019, **29**, 1806006.
10 X. Chen, F. Ren, S. Gu and J. Ye, *Photonics Res.*, 2019, **7**, 381–415.
11 S. M. Hatch, J. Briscoe and S. Dunn, *Adv. Mater.*, 2013, **25**, 867–871.
12 M. Chen, L. Hu, J. Xu, M. Liao, L. Wu and X. Fang, *Small*, 2011, **7**, 2449–2453.
13 X. Li, C. Gao, H. Duan, B. Lu, X. Pan and E. Xie, *Nano Energy*, 2012, **1**, 640–645.
14 Y. Gao, J. Xu, S. Shi, H. Dong, Y. Cheng, C. Wei, X. Zhang, S. Yin and L. Li, *ACS Appl. Mater. Interfaces*, 2018, **10**, 11269–11279.

This journal is © The Royal Society of Chemistry 2020

J. Mater. Chem. C, 2020, **8**, 5409–5416 | **5415**

15 L. Hu, J. Yan, M. Liao, L. Wu and X. Fang, *Small*, 2011, **7**, 1012–1017.

16 H. Chen, L. Hu, X. Fang and L. Wu, *Adv. Funct. Mater.*, 2012, **22**, 1229–1235.

17 J. M. Wu and W. E. Chang, *ACS Appl. Mater. Interfaces*, 2014, **6**, 14286–14292.

18 W. Y. Kong, G. A. Wu, K. Y. Wang, T. F. Zhang, Y. F. Zou, D. D. Wang and L. B. Luo, *Adv. Mater.*, 2016, **28**, 10725–10731.

19 Y. Li, T. Tokizono, M. Liao, M. Zhong, Y. Koide, I. Yamada and J. J. Delaunay, *Adv. Funct. Mater.*, 2010, **20**, 3972–3978.

20 R. Zou, Z. Zhang, Q. Liu, J. Hu, L. Sang, M. Liao and W. Zhang, *Small*, 2014, **10**, 1848–1856.

21 Z. He, Q. Liu, H. Hou, F. Gao, B. Tang and W. Yang, *ACS Appl. Mater. Interfaces*, 2015, **7**, 10878–10885.

22 Z. Hai, M. K. Akbari, C. Y. Xue, H. Y. Xu, L. Hyde and S. Zhuiykov, *Appl. Surf. Sci.*, 2017, **405**, 169–177.

23 K. Huang, Q. Zhang, F. Yang and D. He, *Nano Res.*, 2010, **3**, 281–287.

24 D. L. Shao, M. P. Yu, J. Lian and S. Sawyer, *Opt. Mater.*, 2014, **36**, 1002–1005.

25 D. Li, X. Sun, H. Song, Z. Li, Y. Chen, H. Jiang and G. Miao, *Adv. Mater.*, 2012, **24**, 845–849.

26 M. Peng, Y. Liu, A. Yu, Y. Zhang, C. Liu, J. Liu, W. Wu, K. Zhang, X. Shi and J. Kou, *ACS Nano*, 2015, **10**, 1572–1579.

27 W. Zhang, J. Xu, W. Ye, Y. Li, Z. Qi, J. Dai, Z. Wu, C. Chen, J. Yin and J. Li, *Appl. Phys. Lett.*, 2015, **106**, 021112.

28 P. E. Malinowski, J.-Y. Duboz, P. De Moor, K. Minoglou, J. John, S. M. Horcajo, F. Semond, E. Frayssinet, P. Verhoeve and M. Esposito, *Appl. Phys. Lett.*, 2011, **98**, 141104.

29 R. Dahal, T. Al Tahtamouni, J. Lin and H. Jiang, *Appl. Phys. Lett.*, 2007, **91**, 243503.

30 R. LaPierre, M. Robson, K. Azizur-Rahman and P. Kuyanov, *J. Phys. D: Appl. Phys.*, 2017, **50**, 123001.

31 W. Zheng, R. Lin, Z. Zhang and F. Huang, *ACS Appl. Mater. Interfaces*, 2018, **10**, 27116–27123.

32 H. So, J. Lim and D. G. Senesky, *IEEE Sens. J.*, 2016, **16**, 3633–3639.

33 M. Kumar, H. Jeong, K. Polat, A. Okyay and D. Lee, *J. Phys. D: Appl. Phys.*, 2016, **49**, 275105.

34 M. M. Hou, H. Y. So, A. J. Suria, A. S. Yalamarthy and D. G. Senesky, *IEEE Electron Device Lett.*, 2017, **38**, 56–59.

35 J. Sun, T. Zhan, Z. Liu, J. Wang, X. Yi, P. M. Sarro and G. Zhang, *Appl. Phys. Express*, 2019, **12**, 122007.

36 E. Cicek, R. McClintock, C. Cho, B. Rahnema and M. Razeghi, *Appl. Phys. Lett.*, 2013, **103**, 191108.

37 P. Sandvik, K. Mi, F. Shahedipour, R. McClintock, A. Yasan, P. Kung and M. Razeghi, *J. Cryst. Grow.*, 2001, **231**, 366–370.

38 H.-Y. Liu, Y.-H. Wang and W.-C. Hsu, *IEEE Sens. J.*, 2015, **15**, 5202–5207.

39 S. Butun, T. Tut, B. Butun, M. Gokkavas, H. Yu and E. Ozbay, *Appl. Phys. Lett.*, 2006, **88**, 123503.

40 J. Kim, M.-H. Ji, T. Detchprohm, J.-H. Ryou, R. D. Dupuis, A. K. Sood and N. K. Dhar, *IEEE Photonics Technol. Lett.*, 2015, **27**, 642–645.

41 J. Zheng, L. Wang, X. Wu, Z. Hao, C. Sun, B. Xiong, Y. Luo, Y. Han, J. Wang and H. Li, *Appl. Phys. Lett.*, 2016, **109**, 241105.

42 C. Bayram, J. Pau, R. McClintock and M. Razeghi, *Appl. Phys. Lett.*, 2008, **92**, 241103.

43 Q. Cai, W. Luo, Q. Li, M. Li, D. Chen, H. Lu, R. Zhang and Y. Zheng, *Appl. Phys. Lett.*, 2018, **113**, 123503.

44 P. J. Snyder, R. Kirste, R. Collazo and A. Ivanisevic, *Small*, 2017, **13**, 1700481.

45 R. Calarco, M. Marso, T. Richter, A. I. Aykanat, R. Meijers, A. Hart, T. Stoica and H. Lüth, *Nano Lett.*, 2005, **5**, 981–984.

46 Y.-H. Lee, J.-H. Kang and S.-W. Ryu, *Thin Solid Films*, 2013, **540**, 150–154.

47 Y. Wang, Z. Liao, G. She, L. Mu, D. Chen and W. Shi, *Appl. Phys. Lett.*, 2011, **98**, 203108.

48 J. Xu, D. You, Y. Tang, Y. Kang, X. Li, X. Li and H. Gong, *Appl. Phys. Lett.*, 2006, **88**, 072106.

49 Q. Hou, X. Wang, H. Xiao, C. Wang, C. Yang, H. Yin, Q. Deng, J. Li, Z. Wang and X. Hou, *Appl. Phys. Lett.*, 2011, **98**, 102104.

50 K. Liu, M. Sakurai, M. Aono and D. Shen, *Adv. Funct. Mater.*, 2015, **25**, 3157–3163.

51 S. Jeon, S.-E. Ahn, I. Song, C. J. Kim, U.-I. Chung, E. Lee, I. Yoo, A. Nathan, S. Lee and K. Ghaffarzadeh, *Nat. Mater.*, 2012, **11**, 301.

52 H. Zhou, L. Cong, J. Ma, B. Li, M. Chen, H. Xu and Y. Liu, *J. Mater. Chem. C*, 2019, **7**, 13149–13155.

53 J. Sun, T. Zhan, Z. Liu, J. Wang, X. Yi, P. M. Sarro and G. Zhang, *Opt. Express*, 2019, **27**, 36405–36413.

54 J. Sun, R. Sokolovskij, E. Iervolino, F. Santagata, Z. Liu, P. M. Sarro and G. Zhang, *IEEE Trans. Electron Devices*, 2019, **66**, 4373–4379.

55 B. Zhao, F. Wang, H. Chen, L. Zheng, L. Su, D. Zhao and X. Fang, *Adv. Funct. Mater.*, 2017, **27**, 1700264.

56 Y.-C. Chen, Y.-J. Lu, C.-N. Lin, Y.-Z. Tian, C.-J. Gao, L. Dong and C.-X. Shan, *J. Mater. Chem. C*, 2018, **6**, 5727–5732.

57 Z. H. Zaidi and P. A. Houston, *IEEE Trans. Electron Devices*, 2013, **60**, 2776–2781.

58 Z.-D. Huang, W. Y. Weng, S. J. Chang, C.-J. Chiu, T.-J. Hsueh and S.-L. Wu, *IEEE Sens. J.*, 2013, **13**, 3462–3467.

59 L. Li, Z. Liu, L. Wang, Y. Liu and J.-P. Ao, *Mater. Sci. Semicond. Process.*, 2018, **76**, 61–64.

60 S. Kumar, A. S. Pratiyush, S. B. Dolmanan, S. Tripathy, R. Muralidharan and D. N. Nath, *Appl. Phys. Lett.*, 2017, **111**, 251103.

61 N. Aggarwal, S. Krishna, A. Sharma, L. Goswami, D. Kumar, S. Husale and G. Gupta, *Adv. Electron. Mater.*, 2017, **3**, 1700036.

62 X. Zhang, Q. Liu, B. Liu, W. Yang, J. Li, P. Niu and X. Jiang, *J. Mater. Chem. C*, 2017, **5**, 4319–4326.

63 P. Li, H. Shi, K. Chen, D. Guo, W. Cui, Y. Zhi, S. Wang, Z. Wu, Z. Chen and W. Tang, *J. Mater. Chem. C*, 2017, **5**, 10562–10570.

64 M. Zhang, Y. Wang, F. Teng, L. Chen, J. Li, J. Zhou, X. Pan and E. Xie, *Mater. Lett.*, 2016, **162**, 117–120.

65 A. D. L. Bugallo, L. Rigutti, G. Jacopin, F. Julien, C. Durand, X. Chen, D. Salomon, J. Eymery and M. Tchernycheva, *Appl. Phys. Lett.*, 2011, **98**, 233107.

5416 | *J. Mater. Chem. C*, 2020, **8**, 5409–5416

This journal is © The Royal Society of Chemistry 2020